Geophys. J. Int. (2004) **157,** 1359–1376 doi: 10.1111/j.1365-246X.2004.02257.x

Stresses induced in continental lithospheres by axisymmetric spherical convection

Samuel L. Butler[1] and Gary T. Jarvis[2]

[1]*Department of Geological Sciences, University of Saskatchewan, Saskatoon, Saskatchewan, Canada,* S7K 5E2. *E-mail: sam.butler@usask.ca*
[2]*Department of Earth and Atmospheric Science, York University, Toronto, Ontario, Canada,* M3J 1P3. *E-mail: jarvis@yorku.ca*

Accepted 2004 January 29. Received 2003 December 15; in original form 2003 March 23

SUMMARY

We employ an axisymmetric spherical shell model of mantle convection to examine the magnitude of deviatoric tensile stresses generated in a stationary continental plate resulting from the subduction of oceanic plate material below an active continental margin. The model includes depth-dependent physical properties, uniform internal heating, compressibility and mineral phase-change boundaries at depths of 400 and 660 km. Below 100 km, mantle viscosity is assumed constant. Above 100 km, plate-like behavior may be approximated in axisymmetric spherical geometry by imposing (i) a factor of 10 viscosity contrast between the upper 100 km and the underlying mantle and (ii) a small variation of surface velocity within each plate such that plate mass is conserved and significant vertical mass flux at the base of the plates is therefore confined to the near vicinity of the plate boundaries. We find surface stresses generated by counterflow under our model continental margins is insufficient to actively rift a supercontinent in all but one case. Earth-like curvature appears to be a major factor in reducing surface stresses relative to those found previously in constant viscosity models in plane layer geometry. A simple internal loading model allows us to estimate this effect as a 20 per cent average reduction in stress generation. This suggests that continental rifting requires the pre-existence of localized zones of weakness.

Key words: convection, lithosphere, mantle, stress, supercontinent.

1 INTRODUCTION

Continental rifting and seafloor spreading, followed by a reassembly of continental fragments, seems to have occurred in recurring episodes for at least the past 2.5 billion years (e.g. Condie 1998). The stresses required to rift a large supercontinent and thereby renew this episodic behavior must be generated within the Earth. The question of the precise origin of these stresses, however, remains unclear: in fact, it has been a matter of debate for the past three decades. The debate normally centers on whether rifting is the result of an active mechanism, such as a mantle plume rising directly below the incipient rift, or a passive mechanism, such as regional lateral stresses associated with plate tectonics (generated elsewhere). This distinction characterized the early explanations for seafloor spreading [e.g. McKenzie (1967) vs. Oxburgh & Turcotte (1968)], later models for formation of sedimentary basins [e.g. Bott (1976) and McKenzie (1978), vs. Haxby *et al.* (1976)], the suggested origins of continental flood basalts [e.g. Sheth (1999) vs. Nikishin *et al.* (2002)] and recent discussions of the origins of specific continental rifts such as the Baikal rift zone [e.g. Lesne *et al.* (1998) and Ionov (2002), vs. Ghebreab *et al.* (2002)]. It seems likely to us that both active and passive rifting occurs on continents. For example the large regional swell under parts of the East African rift zone and the Afar triangle may well be the result of the active impact of a mantle plume, whereas the linear rifting along the Red Sea and the Gulfs of Suez, Aqaba and Aden, apparently radiating outwards from Afar appear to be examples of passive rifting.

Passive rifting is expected to occur along pre-existing lines of weakness in the crust, possibly involving the reactivation of palaeofault zones. In contrast, active rifting could conceivably occur anywhere that a rising plume generated sufficient lateral stresses at the surface. Regardless of the type of rifting, lateral stresses within the lithosphere and crust must ultimately arise from vertically acting body forces resulting from gravity within the Earth. Differential vertical forcing in the mantle results in horizontal pressure gradients that, through viscous coupling, generate wide regions of convective circulation. The resulting deviatoric lateral stresses in the lithosphere would naturally be largest directly above stagnation points where vertically rising mantle plumes impact the base of the plates and diverge horizontally. In a series of papers Lowman & Jarvis (1993, 1995, 1996, 1999) extended an initial study by Gurnis (1988) to examine the issue of stresses generated in the lithosphere by the underlying mantle convective circulation. These authors employed 2-D Cartesian models of convection in a constant viscosity mantle, with rigidly moving continental and oceanic plates, which, except at their edges, were of uniform cohesive strength. They

found that diverging flow, in their models, was capable of generating mean deviatoric tensile stresses within the lithosphere greater than 80 MPa, which was deemed sufficient to actively rift a supercontinent. We feel this conclusion is sufficiently important to warrant further investigation. It is based upon model results of uniform-property plane-layer models of mantle convection with internal heat sources. Neither the effects of spherical geometry of the Earth's mantle, compressibility and depth dependence of physical variables were included, nor were the effects of the major mantle phase changes.

In the present study we have examined convection in an axisymmetric spherical shell and conducted a systematic study of the influence of depth-dependent physical properties, compressibility, phase-change boundaries and curvature on the magnitude of deviatoric tensile stresses generated in model continents at the Earth's surface. Our goals are to determine which of these factors influence lithospheric stresses most significantly and whether lithospheric stresses sufficient to rift a continent can be generated in this set of models, which more closely approximates conditions in Earth's mantle. We maintain the same basic viscosity structure that was used in the previous studies: rigidly moving plates overlying a constant viscosity mantle. While this is clearly a simplification, an investigation of all possible rheologies of the plates and mantle is beyond the scope of this study. The assumption of axisymmetry in our model restricts the number of possible flow solutions compared to calculations done in 3-D geometry. Moreover, anomalously vigorous plumes may occur at the poles as in one of the simulations we present. However, the computational efficiency inherent in the use of axisymmetric geometry allows us to make many model runs over times similar to the age of the Earth and preserves the aspect of spherical geometry that area increases, like the radius squared. Vangelov & Jarvis (1994) and Jarvis *et al.* (1995) have shown that this aspect dominates the thermal structure and accounts for the major thermal differences between flow solutions obtained in spherical, cylindrical and planar geometries. This same aspect will be shown here to account for the major difference in surface stresses generated in spherical and Cartesian geometries.

We consider two basic scenarios defined in terms of the location of a single stationary continental plate surrounded by oceanic plates. In the first scenario we consider a circular continental plate of radius 6000 km centered on one pole of the coordinate system (arbitrarily designated north) and initiate a pattern of mantle convection such that an oceanic plate moves northwards towards the stationary continent and subducts under the continental margin. The resulting counterflow under the continent consists of an upwelling along the axis of the coordinate system beneath the north pole. Because of the imposed axisymmetry the upwelling has the form of a cylindrical plume. In the second scenario we consider a stationary, globe encircling, belt of continental mass centered on the equator of the model coordinate system and initiate a pattern of convection such that an oceanic plate moving away from the north pole converges with the northern margin of the continental torus at the equator. This results in a counterflow below our model supercontinent, which takes the form of a sheet-like upwelling. The first scenario allows us to consider cylindrical upwelling plumes, thought to be characteristic of upwellings in the Earth's spherical shell mantle (Bercovici *et al.* 1989a,b). We will therefore concentrate on this scenario. The second scenario, however, is a closer spherical analogue to the 2-D plane layer model of Lowman and Jarvis with sheet-like upwelling plumes. Consequently, we will briefly consider this scenario in order to isolate differences between the earlier plane-layer results and our new spherical-shell results.

We employ the numerical model of Butler & Peltier (2000), which is based on the constant viscosity model of Solheim & Peltier (1994) modified here to incorporate plate-like surface motions. These models are described in the following two sections. As an aid in our interpretation of the numerical results, we also consider a simple internal loading model to compute instantaneous flow and deviatoric stresses under various conditions. This approach is described in Section 4 below.

2 MATHEMATICAL FORMULATION

2.1 Governing equations

In non-dimensional form, the equations governing convection in an infinite Prandtl number, anelastic fluid including the effects of phase transitions and depth-dependent properties can be written in terms of equations describing mass conservation,

$$\nabla \cdot (\rho_r \mathbf{u}) = \rho_r \frac{\partial u_r}{\partial r} + \rho_r \frac{2}{r} u_r + \rho_r \frac{\cot\theta}{r} u_\theta + \rho_r \frac{1}{r} \frac{\partial u_\theta}{\partial \theta} + u_r \frac{\partial \rho_r}{\partial r} = 0, \tag{1}$$

momentum conservation,

$$0 = -\rho g \hat{\mathbf{r}} - \nabla p + \alpha_0 \Delta T[-\nabla \times (\eta \nabla \times \mathbf{u}) + \frac{4}{3}\nabla(\eta \nabla \cdot \mathbf{u}) + 2\nabla(\mathbf{u} \cdot \nabla \eta) - 2(\mathbf{u} \cdot \nabla)\nabla\eta - 2\nabla\eta\nabla \cdot \mathbf{u}], \tag{2}$$

energy conservation,

$$\begin{aligned} DT/Dt - (\tau_0/\alpha_0 \Delta T c_\mathrm{p}) D/Dt(l_1\Gamma_1 + l_2\Gamma_2) = (\kappa/Ra)[\nabla^2 T + (1/k)(\partial k/\partial r)(\partial T/\partial r)] \\ + \mu/(c_\mathrm{p} Ra) + \tau_0 \Phi/(\rho_\mathrm{r} c_\mathrm{p}) - \tau_\mathrm{r} u_\mathrm{r}(T + T_\mathrm{s}), \end{aligned} \tag{3}$$

and an equation of state,

$$\rho = \rho_\mathrm{r}[1 - \alpha_0 \Delta T \alpha (T - T_\mathrm{r}) + 1/K_\mathrm{S}(p - p_\mathrm{r})] + \Delta\rho_1(\Gamma_1 - \Gamma_{1\mathrm{ref}}) + \Delta\rho_2(\Gamma_2 - \Gamma_{2\mathrm{ref}}). \tag{4}$$

In the above system, subscript r denotes a depth-dependent quantity, whereas r represents the radial coordinate, $\mathbf{u}$ is the velocity field, and p, ρ and T are the pressure, density and temperature fields, respectively. Subscript zero is employed to denote a constant reference value used for non-dimensionalization purposes. Φ represents the heat generated by viscous dissipation. The symbols α, η, c_p, K_s and κ represent the thermal expansivity, viscosity, heat capacity, adiabatic bulk modulus and thermal diffusivity of the mantle material, respectively. The depth variation of the various parameters used in our model is shown in Fig. 1.

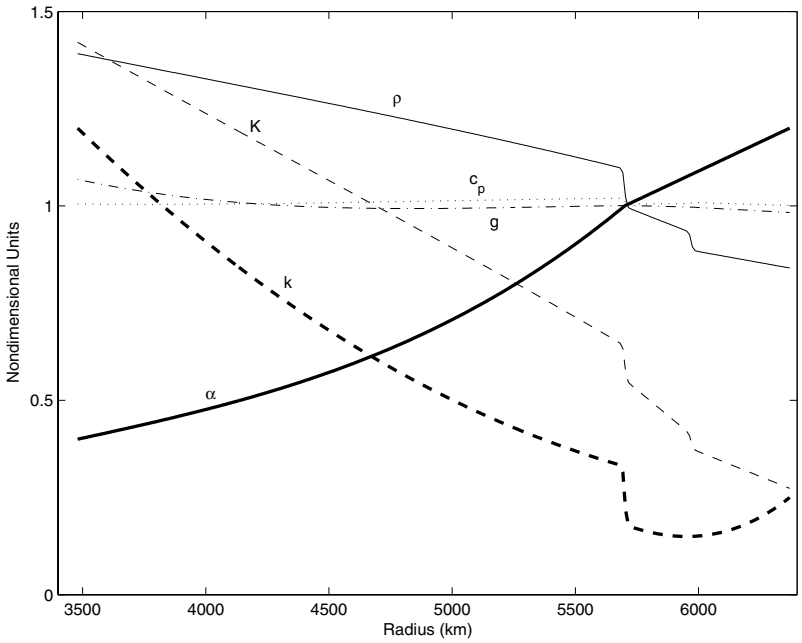

Figure 1. The non-dimensional radial variation of the parameters used in our model calculations. To dimensionalize, multiply the density (thin solid line) by $\rho_0 = 4000$ kg m^{-3}, the thermal expansivity (thick solid line) by $\alpha_0 = 2.5 \times 10^{-5}$ K^{-1}, the thermal conductivity (thick dashed line) by $k_0 = 10$ W/(m K), the adiabatic bulk modulus (thin dashed line) by $K_{S0} = 4.624 \times 10^{11}$ Pa, the specific heat capacity (dotted line) by $c_{p0} = 1250$J/(kg K) and the acceleration as a result of gravity (dot-dashed line) by $g_0 = 10$ m s^{-2}. The CMB temperature is 4000 K.

The non-dimensional parameters in the above system of equations include the Rayleigh number,

$$Ra = \alpha_0 \Delta T g_0 d^3 \rho_0 / (\kappa_0 \eta_0), \tag{5}$$

the dissipation numbers,

$$\tau_0 = g_0 \alpha_0 d / c_{\mathrm{p}0} \quad \text{and} \quad \tau_{\mathrm{r}} = \tau_0 g \alpha / c_{\mathrm{p}}, \tag{6}$$

and the non-dimensional constant internal heating rate per unit volume,

$$\mu = \rho_0 \chi d^2 / k_0 \Delta T. \tag{7}$$

In the definitions of these parameters, d represents the thickness of the mantle. ΔT is the temperature drop, taken to be 3700 K, from the core–mantle boundary (CMB) to the Earth's surface and the Rayleigh number, taken to be 1.12×10^7. χ is the internal heating rate per unit mass.

Effects resulting from the phase transitions are included through the phase density functions

$$\Gamma_i = 1/2\{1 + \tanh[(r_{\mathrm{p}i} - r)h_i]\}, \tag{8}$$

with subscripts $i = 1$ and *2* denoting the phase transitions at 400 and 660 km depth. h_i $(i = 1, 2)$ is a dimensionless width parameter representing the thickness of the divariant phase loop of the ith phase transition and we use $h_1 = h_2 = 400$. In eq. (3) the l_i represent latent heat per unit mass, while in eq. (4), $\Delta\rho_i$ represents the difference in density between the upper and lower phases. The $\Gamma_{i\mathrm{ref}}$ represents the phase boundary functions for a phase transition fixed at its average position. We use $\Delta\rho_1 = 200$ kg m^{-3} and $\Delta\rho_2 = 440$ kg m^{-3}. The symbol $r_{\mathrm{p}i}$ represents the position of the phase boundary and is a function of the polar coordinate of the axisymmetric spherical model geometry and time. Its value must be determined in each angular grid column and for each time step. This may be accomplished by assuming constant Clapeyron slopes. The Clapeyron slopes γ_i for the 400- and 660-km phase transitions, when these effects were turned on, were taken to be 3 and -2.8 MPa K^{-1} (e.g. Chopelas *et al.* 1994). The latent heats are related to the Clapeyron slopes through the Clausius–Clapeyron relation

$$\gamma_i = \rho^2 l_i / (\Delta\rho_i T). \tag{9}$$

It is also useful to ensure that only a single time derivative appears in the energy equation and this was achieved by introducing a transformed temperature, A, such that

$$A = T - \tau_0 / (\alpha_0 \Delta T c_{\mathrm{p}}) \, (l_1 \Gamma_1 + l_2 \Gamma_2). \tag{10}$$

The momentum conservation equation can be written in terms of a stream function ψ and vorticity ω as

$$\frac{\partial^2 \psi}{\partial r^2} r^2 \sin\theta - \frac{\partial \psi}{\partial r} \frac{1}{\rho_r} \frac{\partial \rho_r}{\partial r} r^2 \sin\theta + \frac{\partial^2 \psi}{\partial \theta^2} \sin\theta - \frac{\partial \psi}{\partial \theta} \cos\theta = -\omega \rho_r r^2 \sin\theta \tag{11}$$

and

$$\frac{\partial^2\omega}{\partial r^2}r^2\sin\theta + \frac{\partial\omega}{\partial r}r^2\sin\theta\left(\frac{g\rho_r}{K_S}\right) + \frac{\partial^2\omega}{\partial\theta^2}\sin\theta - \frac{\partial\omega}{\partial\theta}\cos\theta$$
$$= \frac{\rho_r g\alpha r^2\sin^2\theta}{\eta}\left\{\frac{\partial A}{\partial\theta} + \frac{2h_1\Gamma_1(1-\Gamma_1)}{\alpha_0\Delta T}\left(\frac{l_1\tau_0}{c_p} - \frac{\Delta\rho_1}{\rho_r\alpha}\right)\frac{\partial r_{p1}}{\partial\theta} + \frac{2h_2\Gamma_2(1-\Gamma_2)}{\alpha_0\Delta T}\left(\frac{l_2\tau_0}{c_p} - \frac{\Delta\rho_2}{\rho_r\alpha}\right)\frac{\partial r_{p2}}{\partial\theta}\right\} \quad (12)$$
$$+ \frac{4g}{3K_S\rho_r}\frac{\partial\rho_r}{\partial r}\left(\frac{\partial^2\psi}{\partial\theta^2}\sin\theta - \frac{\partial\psi}{\partial\theta}\cos\theta\right),$$

where

$$u_r = \frac{1}{\rho_r r^2\sin\theta}\frac{\partial\psi}{\partial\theta}, u_\theta = \frac{-1}{\rho_r r\sin\theta}\frac{\partial\psi}{\partial r} \quad (13)$$

and

$$\omega = r\sin\theta\nabla\times\mathbf{u}\cdot\hat{\phi}. \quad (14)$$

2.2 Boundary Conditions

In order to incorporate the effects of surface plates we impose a viscosity jump by a factor of 10 across an interface at a depth of 100 km. This discontinuity in viscosity results in discontinuities in the vorticity and its first derivative. As a result, we solve eqs (11) and (12) independently in the upper and lower layers and impose the following boundary conditions at the internal interface (in a manner similar to that used by Rabinowicz M. *et al.* 1990; Monnereau & Rabinowicz 1996; Dubuffet *et al.* 2000):

$$\Delta\psi = 0, \quad (15)$$

$$\Delta\frac{\partial\psi}{\partial r} = 0, \quad (16)$$

$$\Delta(\eta\omega) = 2\sin\theta\left(u_\theta - \frac{\partial u_r}{\partial\theta}\right)\Delta\eta \quad (17)$$

and

$$\Delta\frac{\partial(\eta\omega)}{\partial r} = 2\sin\theta\left(\frac{\partial^2 u_r}{\partial r\partial\theta} + \frac{1}{\rho_r}\frac{\partial\rho_r}{\partial r}\frac{\partial u_r}{\partial\theta}\right)\Delta\eta. \quad (18)$$

Here Δ represents the operation of subtracting the value on the lower side of the discontinuity from that on the upper side. Eqs (15)–(18) represent continuity of vertical and horizontal velocity, and the tangential and normal stress, respectively, at the base of the lithosphere. These boundary conditions across the viscosity discontinuity at 100 km depth were satisfied by expanding the derivatives in fourth order finite-difference approximations and combining eqs (15) and (16), and (17) and (18), to obtain equations for ψ and ω on each side of the boundary. See Appendix A for a detailed derivation of eqs (15)–(18).

At the lower (inner) boundary of the model (representing the CMB) vanishing radial velocity and shear stress are applied as mechanical boundary conditions, while at the upper (outer) surface of the lithosphere vanishing radial velocity and plate-like azimuthal velocities are imposed. In order that the imposed surface velocities produce a plate-like flow, we require that significant vertical mass flux only occur at the plate boundaries. This may be achieved by employing a surface velocity profile of the form

$$u_\theta = \sum_i^n \frac{u_{0i}}{2\sin(\theta)}\{\tan h[h_t(\theta-\theta_{i1})] - \tan h[h_t(\theta-\theta_{i2})]\}, \quad (19)$$

where the u_{0i} are constants that indicate the area weighted velocity of the ith plate, and θ_{i1} and θ_{i2} are the north and south boundaries of each plate. h_t is chosen so that the velocity change occurs over four azimuthal grid points. The u_{0i} are determined using the force balance approach of Gable *et al.* (1991) as will be discussed in the next section.

2.3 Numerical technique for representing surface plates

Before we begin evolving the system forwards in time, we find stream-function and vorticity pairs corresponding to the flow field that is driven by the motion of a single surface plate only. This is done by setting one of the u_{0i} to a non-zero value with the others set to zero and by removing buoyancy effects resulting from temperature and phase boundary fluctuations in the interior [setting the A and r_{pi} dependent terms on the right-hand side of eq. (12) equal to 0]. In the simulations reported herein, the continental plate is immobile and there are two other moving plates. For each of the moving plates, the stream-function–vorticity pairs found in this way are ψ_1, ω_1 and ψ_2, ω_2. As we evolve the system forwards in time, eqs (11) and (12) are solved for the case of a non-slip surface boundary condition and with the buoyancy terms included to yield $\psi_{\rm nsl}$ and $\omega_{\rm nsl}$ at each time step. The stream function and vorticity at a given time step are then given by a linear superposition

$$\psi = c_1\psi_1 + c_2\psi_2 + \psi_{\rm nsl},$$
$$\omega = c_1\omega_1 + c_2\omega_2 + \omega_{\rm nsl}, \quad (20)$$

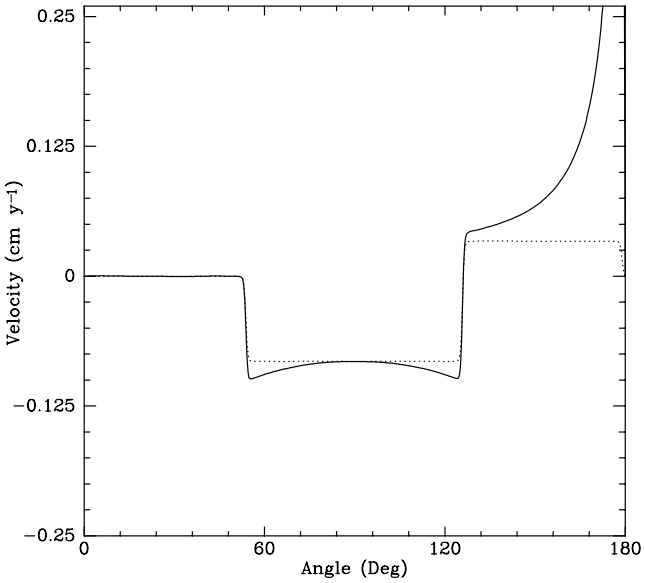

Figure 2. Snapshot of the azimuthal surface velocity (solid line) and area weighted surface velocity, $u_\theta \sin(\theta)$ (dotted line) as a function of the azimuthal angle from model I.3.

where the coefficients c_1 and c_2, which determine the plate velocities, are chosen so that the integral of the tangential stress on the base of each of the moving plates is zero. The tangential stress depends linearly on the stream-function and the vorticity so that c_1 and c_2 can be obtained at each time step from the solution of

$$\begin{pmatrix} \overline{\tau_{r\theta}}_{1,1} & \overline{\tau_{r\theta}}_{1,2} \\ \overline{\tau_{r\theta}}_{2,1} & \overline{\tau_{r\theta}}_{2,2} \end{pmatrix} \begin{pmatrix} c_1 \\ c_2 \end{pmatrix} + \begin{pmatrix} \overline{\tau_{r\theta}}_{1,\mathrm{nsl}} \\ \overline{\tau_{r\theta}}_{2,\mathrm{nsl}} \end{pmatrix} = \begin{pmatrix} 0 \\ 0 \end{pmatrix}. \tag{21}$$

Here $\overline{\tau_{r\theta}}_{i,j}$ represents the area integral of the tangential stress on the base of plate i as a result of flow field j.

Solutions of eqs (11) and (12) were obtained using the elliptic multigrid solver MUDPAC (Adams 1993). As a result of the nature of the boundary conditions and the presence of compressibility and depth-dependent properties, the equations were iterated until convergence to a final solution was obtained at each time step. The grid used had 513 × 257 azimuthal and radial grid points in the sublithospheric mantle and 513 × 9 grid points in the lithosphere.

2.4 Model set-up

A fixed plate configuration was used for each of the two scenarios described above. In scenario I, the surface plate configuration was chosen to mimic the situation of a single supercontinent surrounded by a continuous subduction zone (as per the late Permian Pangea–Gondwana assemblage). A single, immobile circular plate of radius 6000 km, meant to represent the supercontinent, was placed at one pole of the spherical coordinate system (that was arbitrarily designated the north pole). It extends to a colatitude of $\theta = 54^\circ$ from the pole. Two oceanic plates, which were allowed to move under the influence of convective motion in the mantle, covered the remainder of the surface. One of these comprised an equatorial belt of width 8,000 km; the other formed a circular cap of radius 6,000 km at the other geometric pole. The initial temperature field was taken from a calculation with a free-slip surface boundary condition that was run with a similar Rayleigh number. At the onset of the simulation, the equatorial plate moved northwards towards the stationary north polar plate. Fig. 2 shows a profile of the surface velocity from $\theta = 0^\circ$ to 180° for the model called I.3 after the model had been running for some time. From $\theta = 0^\circ$ to 54° (the supercontinent zone) we see $u_\theta = 0$. From $\theta = 54^\circ$ to 126° surface velocity is negative, or northward, while for $\theta = 126^\circ$ to 180° surface velocities are positive, or southward. The large northward-moving equatorial plate shows small variations in u_θ, as per eq. (19), in order to confine vertical mass flux (into and out of) the plate to the vicinity of the plate boundaries, while conserving mass within the plate as it moves into regions of different total surface area. Because these velocity variations are small we believe the essence of a rigid plate is captured and that their effect on the calculated surface stresses is small. The same cannot be said of the southern plate: because it moves into regions of extreme change in surface area, the surface velocity prescribed by our formulation bears no resemblance to a rigid plate. Consequently, we focus our attention on the interaction of the northbound equatorial plate and the stationary polar plate. Figs 3 and 4 depict contours of temperature and azimuthal velocity at one instant of model I.3 described in the next section. These are typical of scenario-I models, with convergence and subduction of the northbound plate material at the southern margin of the stationary (continental) plate and divergence occurring at the southern plate boundary. A key feature here is the counter flow induced below the stationary continental plate as a consequence of subduction

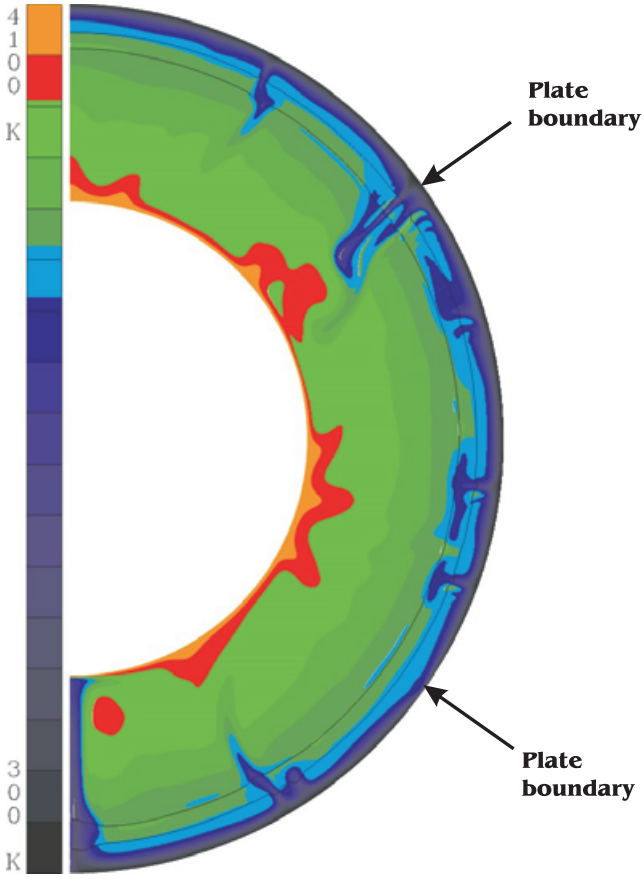

Figure 3. Snapshot of the temperature from model I.3 for the same instant in time as Fig. 2. Light black lines indicate the positions of the 400 and 660 km depth phase changes. The positions of the plate boundaries are indicated.

of the northbound (oceanic) plate. This is most clearly revealed in the velocity contours, which show a large southward component of flow under the continental plate.

In the scenario-II models, the plate that is centered on the geometric equator was designated the continental plate and assigned a velocity of zero. Both polar plates were allowed to move and we initiated convection such that both polar plates moved so as to converge with the margins of the equatorial continent. As noted above, the polar plate does not have a constant surface velocity but, nevertheless, does conserve mass and avoids any radial influx of material. In both scenarios, the only difference between our continental and oceanic plates is that the continental plates are immobile while the oceanic plates move in response to the underlying flow.

A series of models were run with various variations in physical properties in order to investigate their effects on surface stresses. These are summarized in Table 1. Model I.1 is a complete model with compressibility, internal heating, depth-dependent properties and two mineral phase change boundaries at nominal depths of 400 and 660 km. These aspects of the model are described in detail by Butler & Peltier (2000). The principal difference here is the inclusion of the high-viscosity continental and oceanic plates. Below the plates a constant viscosity is assumed for the sake of comparison with the constant viscosity models of Lowman & Jarvis (1999). In all but one model (I.3) the assumed value was 88×10^{21} Pa s. This large viscosity, which was necessary for computational efficiency, results in the effective Benard–Rayleigh number for these simulations being 5×10^5, somewhat lower than the real Earth as is evidenced by the surface velocities, listed in Table 2, which are more than an order of magnitude lower than plate velocities. Models I.2 to I.5 are similar to model I.1 except that, respectively, no internal heat sources are included, viscosity is reduced by a factor of three everywhere, the effects of mineral phase transitions have been removed and the effects of compressibility and depth-dependent quantities have been removed. Models II.1 and II.2 were run with a continental belt at the equator without the effects of phase transitions and with and without the effects of compressibility and depth-dependent properties, respectively.

Each of these models was run for dimensional times similar to the age of the Earth. There were no significant statistical differences in the measured stresses between the beginning and ending of the simulations indicating that model spin-up effects were likely not significant. At each time step, the diagonal stresses, σ_{rr}, $\sigma_{\theta\theta}$ and $\sigma_{\phi\phi}$ were computed throughout the continental plate. In spherical axisymmetric geometry, the normal stress perpendicular to the model domain, $\sigma_{\phi\phi}$, is not identically 0. However, it was found to be very small in magnitude at all times compared with the other two normal stresses. As a result, the continent could be said to experience horizontal tensile stress wherever $\sigma_{\theta\theta} - \sigma_{rr} > 0$. Following Lowman & Jarvis (1999) we average this quantity over the depth of the plate and find the lateral coordinate where

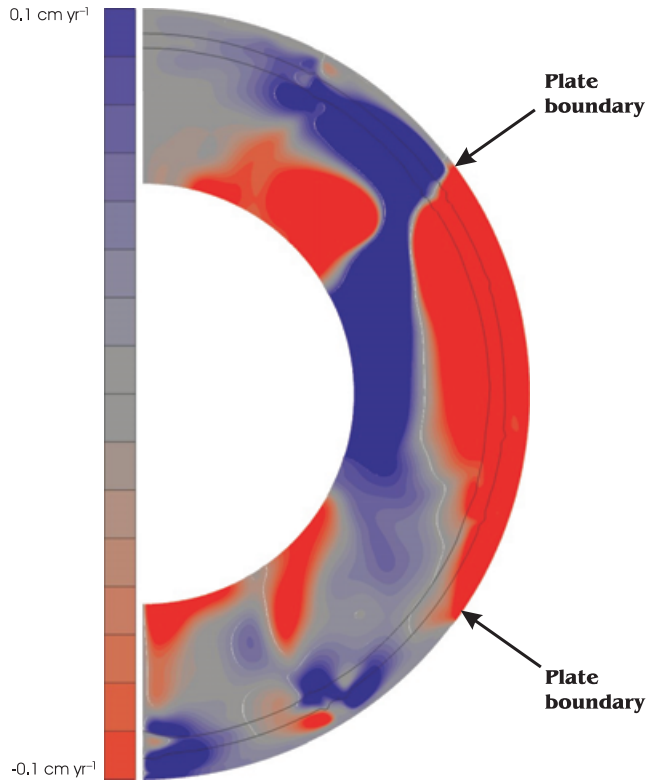

Figure 4. Snapshot of the azimuthal velocity from model I.3 for the same instant in time as Figs 2 and 3. Light black lines indicate the positions of the 400 and 660 km phase changes. Positive velocity means southward.

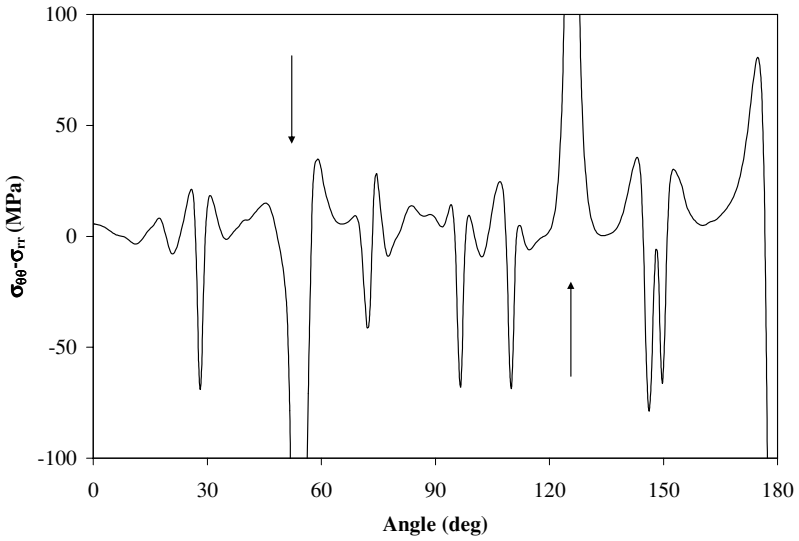

Figure 5. Snapshot of $\sigma_{\theta\theta} - \sigma_{rr}$ as a function the of azimuthal angle from model I.3 for the same time as the plots shown in Figs 2, 3 and 4. Arrows indicate the positions of the plate boundaries.

this depth-averaged value is a maximum. We expect fracture and rifting to occur if this maximum value, designated $\sigma_{\max}$, exceeds the yield strength of the lithosphere. Based on the work of Brace & Kohlstedt (1980) and Kohlstedt *et al.* (1995), Lowman & Jarvis (1999) estimated that a reasonable value for the threshold value for the mean extensional stress was 80 MPa and found that this threshold could be reached in their plane layer uniform property models, with or without internal heating. A similar value of 70 MPa had been used previously by Gurnis (1988).

Table 1. Summary of numerical model runs.

Model run	Continent position	Internal heating	Depth-dependent properties	Phase transitions	Viscosity 10^{21} Pa s	Compressibility
I.1	Pole	20 TW	Yes	Yes	88	Yes
I.2	Pole	0 TW	Yes	Yes	88	Yes
I.3	Pole	20 TW	Yes	Yes	28	Yes
I.4	Pole	20 TW	Yes	No	88	Yes
I.5	Pole	20 TW	No	No	88	No
II.1	Equator	20 TW	Yes	No	88	Yes
II.2	Equator	20 TW	No	No	88	No

Table 2. Time average of flow diagnostics. Kinetic energy is in arbitrary units.

Model run	$\sigma_{\max}$ (MPa)	Standard deviation $\sigma_{\max}$ (MPa)	u_{sur} (cm yr^{-1})	Kinetic energy
I.1	37.4	9.5	0.08	1.7
I.2	40.4	5.8	0.16	3.6
I.3	25.4	7.5	0.09	5.9
I.4	33.1	4.7	0.15	3.6
I.5	72.3	18	0.5	40
II.1	34.3	4.7	0.07	4.4
II.2	42.7	8.5	0.23	2.4

3 MODEL RESULTS

3.1 Scenario I: continental cap at the pole

It is expected that plates will be under tension/compression above up/downwelling plumes bordered by adjacent regions of compression/tension. Stresses can also be generated by long-wavelength flows applying shear stresses to the base of plates. Referring to Figs 3 and 4 once more, we see that there are no active upwellings impinging on the surface plate but there is a cold downwelling sinking from the cold surface boundary layer. There is also a long-wavelength southward-moving flow below the base of the continental plate, which we might expect would cause tension in the plate interior. In Fig. 5 we see a plot of $\sigma_{\theta\theta} - \sigma_{rr}$ as a function of the azimuthal angle for the same instant in time as for the results shown Figs 2, 3 and 4. The two large spikes in the differential stress, with magnitudes of approximately 200 MPa, occur at the plate boundaries (whose positions are indicated by arrows). At the boundary at 54° the boundary is under compression while at 126° it is under tension, consistent with the plates converging and diverging at these locations, respectively. The sinking subcontinental material at 28° causes a compression spike with tension on either side. However, the adjacent regions of tension attain peak amplitudes of stress-difference of only 25 MPa and it can be seen that the stress difference does not approach 80 MPa anywhere within the continental plate.

Fig. 6 displays plots of the value of $\sigma_{\max}$ as a function of time for the first four of our scenario-I models. We also list the average value and standard deviation of $\sigma_{\max}$ for each of the model runs in Table 2, as well as the average surface velocity and kinetic energy for the purpose of comparing the convective vigor of the various calculations. The uppermost curve is the time-series for model I.1. Peak stresses are approximately 60 MPa, some 20 MPa short of the 80 MPa threshold for rifting. None of the variations from model I.1 that are included in the other three models lead to higher peak stresses in the continent. Consistent with the results of Lowman & Jarvis (1999) is the fact that model I.1 with internal heating reaches higher peak stresses and does so more frequently than does model I.2 without internal heating, although the average stress of I.2 is slightly higher. From inspection of Fig. 6 it appears that removing the phase boundaries also decreases the surface stresses somewhat because model I.4 without phase transitions has generally lower stresses than model I.1. Removing phase transitions also has the effect of decreasing the variability of surface stresses as is evidenced by the low standard deviation of I.4 compared with I.1, which we might expect because phase transitions are known to increase the time variability of convective flows (e.g. Christensen & Yuen 1985; Solheim & Peltier 1994). A longer time integration for a model with phase transitions (not shown) indicated some correlation between large surface stresses and significant mass flux across the 660 km phase transition, although none of the excursions were sufficiently large to reach the 80 MPa threshold. One implication of this figure is that increasing the overall viscosity of the mantle should lead to higher surface stresses, because the lower viscosity calculation, I.3, shows significantly lower stresses. However, the viscosity used in model I.1 is already significantly higher than the value of 10^{21}*Pas* used by Lowman & Jarvis (1996); Lowman & Jarvis (1999). Thus the larger stresses found by Lowman & Jarvis (1996, 1999) cannot be attributed to viscosity.

The last Scenario-I model, I.5, was run to assess the importance of compressibility by comparing it with I.4. Neither I.4 nor I.5 have mineral phase boundaries and both have 20 TW of internal heating. Model I.4 retains compressibility and depth-dependent properties, while model I.5 neglects compressibility and depth-dependent properties and is therefore our closest scenario-I analogue to the Boussinesq models of Lowman & Jarvis (1999). In Fig. 7, we plot the time-series of $\sigma_{\max}$ computed from these two models. The Boussinesq model, I.5, rapidly and frequently reaches and exceeds the threshold value of 80 MPa suggested by Lowman & Jarvis (1995), whereas the anelastic-liquid model,

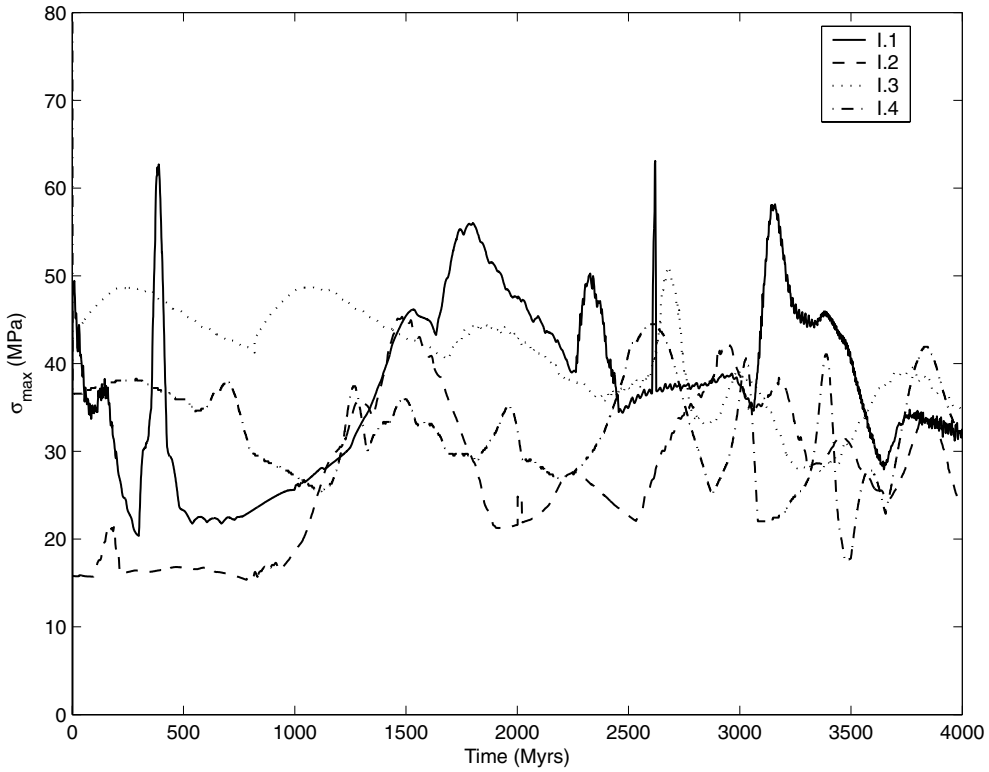

Figure 6. $\sigma_{\max}$ as a function of time for models I.1–I.4 (compressible models with the continent at the pole).

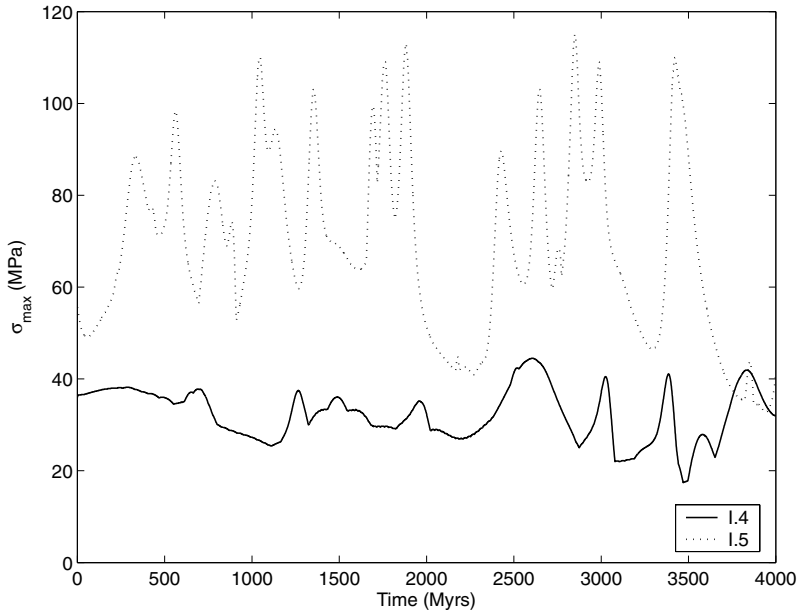

Figure 7. $\sigma_{\max}$ as a function of time for models I.4 and I.5 (comparison of compressible and incompressible models with the continent at the pole).

I.4, generates maximum stress differences that are consistently below this threshold by a factor of two or more. As can be seen in Table 2, simulations I.1–I.4 have similar kinetic energies and hence similar effective Rayleigh numbers, while the kinetic energy in simulation I.5 is significantly higher. This may be attributed to the increased convective forcing as a result of the lack of an adiabatic temperature gradient in the Boussinesq case; the CMB temperature is the same in model I.5, as in the other four models. Also, as can be seen in Fig. 1, the thermal expansivity is significantly reduced near the CMB in models I.1–I.4, significantly reducing the buoyancy of upwelling plumes in these models. This is not the case in the Boussinesq model I.5. Consequently, model I.5 experiences artificially enhanced plumes at the polar axis and the location of the maximum extensional stress within the continental plate is always at the pole. This is not always true for model I.4 with more subdued polar plumes. Rather, it wandered significantly about the continent.

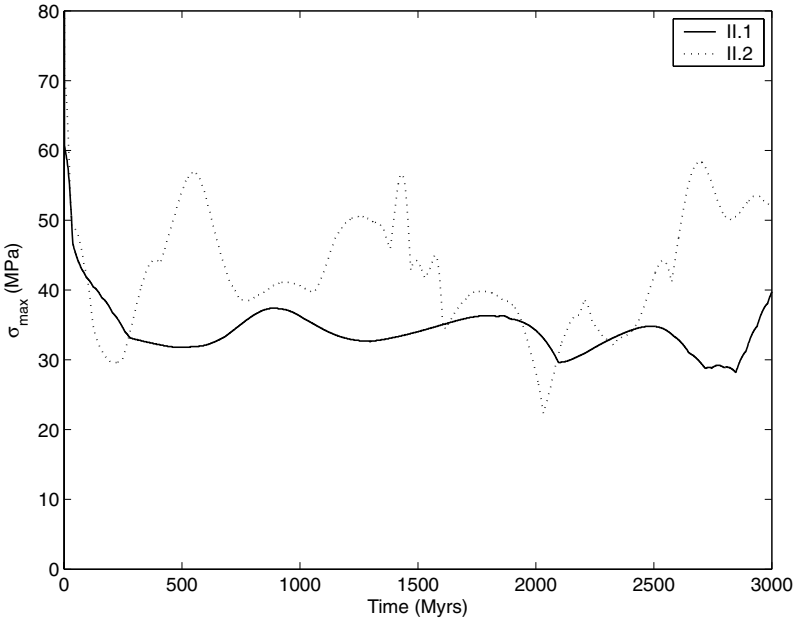

Figure 8. $\sigma_{\max}$ as a function of time for models II.1 and II.2 (comparison of compressible and incompressible models with the continent at the equator).

3.2 Scenario II: continental belt at the equator

In our scenario-II models, the stationary continental plate consists of an equatorial belt, or torus, of 8000 km in width. The northern oceanic plate moves southwards and subducts below the northern margin of the continent, triggering an upwelling sheet below the continental plate. This is the spherical analogue of the 2-D upwelling sheets in the plane layer models of Lowman & Jarvis (1999). Cylindrical plumes, which rise below the continent in the scenario-I models, are precluded from these models. Time-series of the maximum tensile stresses generated in the continental plate are shown in Fig. 8 for two models, II.1 and II.2. These are similar to the scenario-I models I.4 and I.5 shown in Fig. 6; model II.1 being a compressible (i.e. anelastic-liquid) model and model II.2 being an incompressible (i.e. Boussinesq) model. Although the Boussinesq model again develops higher tensile stresses in the continental plate and higher average kinetic energies in the mantle interior than the compressible one, the difference between the two cases is much less pronounced than in the scenario-I models. In fact, the difference in maximum stresses shown in Fig. 8 may be attributed entirely to the decreased vigor of flow in the compressible model caused by the presence of an adiabatic temperature gradient (because the temperature difference across the mantle is the same in both models).

Model II.2 is the closest spherical analogue to the plane layer models of Lowman & Jarvis (1999). Maximum stresses found in this model are approximately 25 per cent lower than in the plane layer models suggesting that the presence of curvature in the mantle acts to reduce the maximum tensile stress, which can be generated in overlying continental plates. In order to further investigate the effects of curvature on surface stress, we develop in the following section a simple internal loading model for a Boussinesq fluid in either a plane layer or a spherical shell of arbitrary curvature.

4 AN INTERNAL LOADING MODEL

In order to further investigate factors affecting the generation of stress differences in a lithospheric plate, we derive simple spectral models in Cartesian and spherical axisymmetric geometry. A schematic of the models is shown in Fig. 9. A wide surface plate is represented by a 100-km thick, high-viscosity region at the surface. We assume a viscosity discontinuity at the base of the plate. The top surface is assumed to be immobile. We calculate the stress difference over the depth of the plate as a result of the flow driven by a temperature perturbation that we introduce at a given depth. In Cartesian geometry, the domain is assumed to be of infinite width and the horizontal variation of the temperature perturbation is sinusoidal, while in spherical geometry the domain extends over 180° and the temperature perturbations vary like Legendre polynomials. Internal loading theory of this type has been used for some time (e.g. Hager & Clayton 1989; Forte & Peltier 1991), usually to predict surface observables caused by convection in the mantle that is driven by density heterogeneities that are inferred from seismic tomography. This approach has been used to calculate stresses at the Earth's surface (e.g. Steinberger *et al.* 2001) and to compare these with the stress pattern observed at the Earth's surface. We use a more simplified, idealized model here because it allows us to efficiently investigate the effects of the magnitude of the viscosity jump, the magnitude of the curvature and the depth of the temperature perturbation.

This simple harmonic analysis may not be strictly applicable to the Earth's mantle because it implicitly incorporates equal amplitudes of hot and cold perturbation about some mean value, whereas in the Earth's mantle cold perturbations originating at the large upper surface would be more pronounced than hot perturbations originating at the smaller lower boundary. Thus larger negative and smaller positive perturbations would be more appropriate at mid-depths. However, these are competing effects that tend to cancel because it is the horizontal gradients of

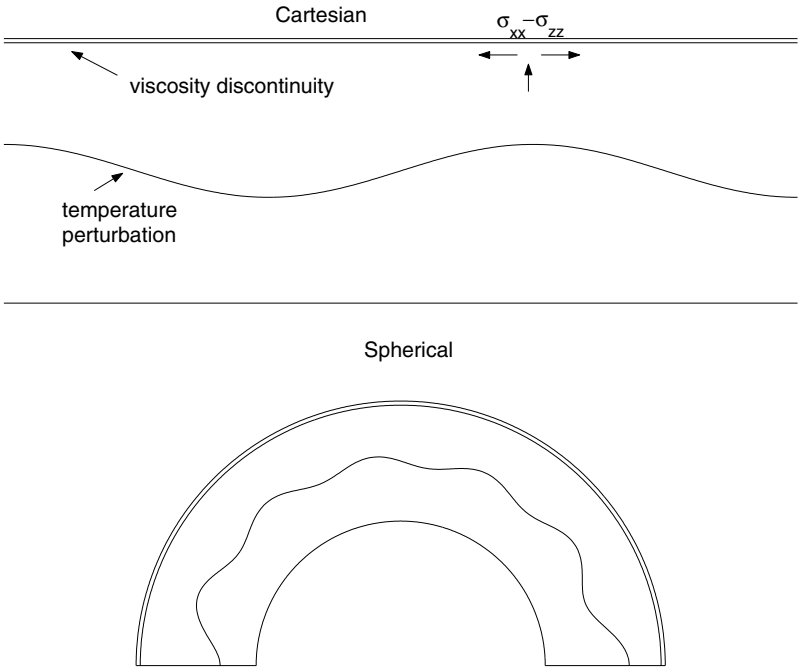

Figure 9. A schematic of the internal loading calculations that were performed. A temperature perturbation that varies horizontally sinusoidally in Cartesian geometry and like a Legendre polynomial in spherical geometry where a delta function variation vertically is imposed (the temperature perturbation is shown to be varying vertically but this is only meant to represent a variation in magnitude). A viscosity jump is imposed at 100 km depth below the surface, which is required to be immobile.

the net perturbations, not absolute values, which drive the flow. Consequently, simple harmonic perturbations generate reasonable estimates of surface stress, sufficient to allow comparisons of results obtained in the two geometries.

4.1 Model formulation

4.1.1 Cartesian geometry

We define a vector

$$\mathbf{y} = (w, w', w'', p/\delta), \tag{22}$$

where w and p are z-dependent functions representing the vertical component of velocity and pressure. The symbol $\delta = \alpha \Delta T$, where α is the thermal expansivity and ΔT is a temperature scale. Primes indicate a derivative with respect to z. The Boussinesq, infinite Prandtl number momentum and continuity equations, when Fourier transformed over the horizontal direction, result in equations of the form

$$\frac{\partial \mathbf{y}}{\partial z} = \mathbf{A}\mathbf{y} + \mathbf{b}, \tag{23}$$

where

$$\mathbf{A} = \begin{pmatrix} 0 & 1 & 0 & 0 \\ 0 & 0 & 1 & 0 \\ 0 & k^2 & 0 & k^2\eta_0/\eta(z) \\ -k^2\eta(z)/\eta_0 & 0 & \eta(z)/\eta_0 & 0 \end{pmatrix}. \tag{24}$$

See Butler & Peltier (1997) for a derivation. The vertical variation in the horizontal velocity, u, is related to the vertical component by the continuity equation, $u = \frac{i}{k} w'$, where $i = \sqrt{-1}$.

Here the viscosity $\eta(z) = \eta_0$ in the bulk of the mantle and $\eta_0 + \Delta\eta$ within the lithosphere. The vector $\mathbf{b}$ is given by

$$\mathbf{b} = (0, 0, 0, T). \tag{25}$$

We take buoyancy-inducing temperature perturbations of the form

$$T = \mathrm{Dir}(z - z_0), \tag{26}$$

where z_0 is the height of the perturbation above the CMB and Dir is the Dirac delta function. Note that this implies that there is no vertical thickness to the temperature perturbation that we introduce. This allows us to unambiguously investigate the effects resulting from the vertical

placement of the anomaly. The total horizontal variation in mass that is induced is the same as if the temperature perturbation were occurring uniformly over the entire depth of the mantle.

The jump conditions at the viscosity discontinuity at the base of the lithosphere are derived based on the continuity of vertical and horizontal velocity, as well as normal and tangential stress. They are given by

$$w_+ = w_-, \tag{27}$$

$$w'_+ = w'_-, \tag{28}$$

$$w''_+ = w''_-\eta_0/(\eta_0 + \Delta\eta) - wk^2\Delta\eta/(\eta_0 + \Delta\eta), \tag{29}$$

$$p_+/\delta = p_-/\delta + 2w'\Delta\eta. \tag{30}$$

The jump condition at the position of the temperature anomaly is given by

$$p_+/\delta = p_-/\delta + 1. \tag{31}$$

We impose conditions of zero vertical velocity at the top and bottom boundaries, zero tangential stress at the bottom boundary and zero horizontal velocity at the surface boundary. It can be shown using the continuity equation that the condition of 0 tangential stress at the bottom can be written as $w'' = 0$ and the condition of zero horizontal velocity at the surface can be written as $w' = 0$.

The average lithospheric stress difference is given by

$$\int_{z_b}^{z_s} \tau_{xx} - \tau_{zz} dz/t_\mathrm{p} = -4(\eta_0 + \Delta\eta)\int_{z_b}^{z_s} w' dz/t_\mathrm{p} = -4(\eta_0 + \Delta\eta)w(z_b)/t_\mathrm{p}, \tag{32}$$

where: t_p is the thickness of the plate; z_b and z_s are the positions of the base of the plate and the upper surface; we have used the continuity equation for a Boussinesq fluid and the boundary condition at z_s to simplify the form of the stress difference.

4.1.2 Spherical axisymmetric

We define the vector

$$\mathbf{y} = (W, W', W'', p/\delta). \tag{33}$$

Following Chandrasehkar 1961, vertical and horizontal velocities u_r, u_θ are related to W by

$$u_r = W P_l(\cos\theta)/r \tag{34}$$

and

$$u_\theta = \frac{W/r + W'}{l(l+1)} \frac{\partial P_l(\cos\theta)}{\partial\theta}, \tag{35}$$

where $P_l(\cos\theta)$ is the Legendre polynomial of order l. The momentum equation becomes

$$\frac{\partial \mathbf{y}}{\partial r} = \mathbf{A_s}\mathbf{y} + \mathbf{b_s}, \tag{36}$$

where

$$\mathbf{A_s} = \begin{pmatrix} 0 & 1 & 0 & 0 \\ 0 & 0 & 1 & 0 \\ -\dfrac{l(l+1)}{r^3} & \dfrac{l(l+1)}{r^2} & -\dfrac{3}{r} & \dfrac{l(l+1)}{r}\eta_0/\eta(r) \\ -\dfrac{l(l+1)}{r^3}\eta(r)/\eta_0 & \dfrac{2}{r^2}\eta(r)/\eta_0 & \dfrac{1}{r}\eta(r)/\eta_0 & 0 \end{pmatrix} \tag{37}$$

and

$$\mathbf{b_s} = (0, 0, 0, T). \tag{38}$$

The jump conditions at the viscosity discontinuity become

$$W_+ = W_-, \tag{39}$$

$$W'_+ = W'_-, \tag{40}$$

$$W''_+ = W''_-\frac{\eta_0}{\eta_0 + \Delta\eta} + \frac{\Delta\eta}{\eta_0 + \Delta\eta}\frac{2 - l(l+1)}{r^2}W, \tag{41}$$

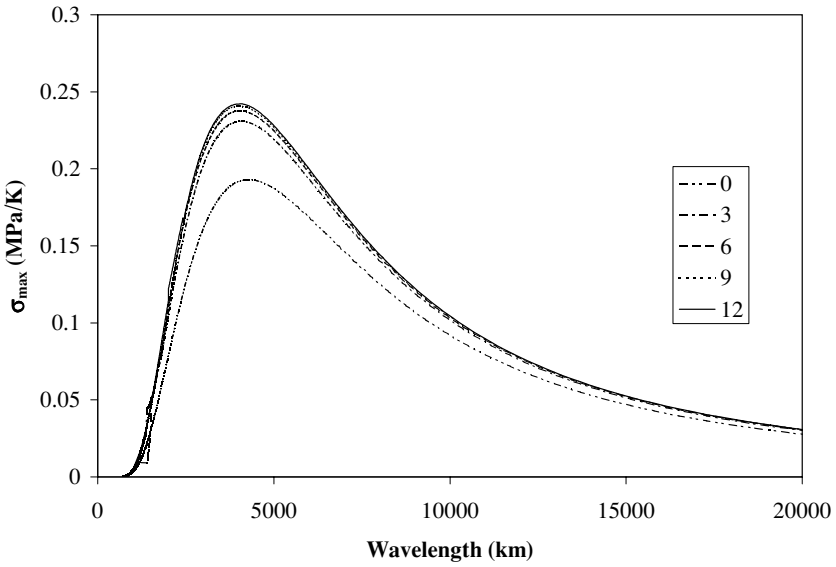

Figure 10. $\sigma_{\max}$ as a function of the horizontal wavelength of the temperature perturbation for various values of the viscosity discontinuity (indicated on the figure) between the interior and the surface plate.

$$p_+/\delta = p_-/\delta + -2\frac{W}{r^2}\Delta\eta + \frac{2W'\Delta\eta}{r}. \tag{42}$$

The breaking stresses at a point within the plate are calculated using the Cartesian approximation to this quantity, which is expected to be adequate considering the small change in radius associated with the thickness of the plate.

4.2 Numerical methodology

The fourth-order equations were solved by first integrating two linearly independent vectors that satisfied the bottom boundary conditions that we chose to be (0, 1, 0, 0) and (0, 0, 0, 1) up to the surface where they had values $\mathbf{y}_1$ and $\mathbf{y}_2$. These solutions were calculated without the discontinuity in pressure (eq. 31) and represent the homogeneous solutions of differential eqs (23) and (36). A third solution starting at the bottom with $\mathbf{y} = (0, 0, 0, 0)$ was integrated through the pressure discontinuity at the position of the temperature perturbation to the surface where it had value $\mathbf{y}_3$. Constants c_1 and c_2 were then found such that the combination $c_1\mathbf{y}_1 + c_2\mathbf{y}_2 + \mathbf{y}_3$ satisfied the surface boundary conditions of $w = 0$ and $w' = 0$. A fourth-order Runge–Kutta scheme was used to perform the integrations. For the spherical calculations, the equations were integrated from the lower boundary, r_c, to the upper boundary, r_s. The ratio r_s/r_c defines the curvature of the layer.

4.3 Results and implications

In order to determine the magnitude of the viscosity discontinuity that was necessary for the plate to behave essentially rigidly, we repeated a series of internal loading, Cartesian calculations with different values of the viscosity jump between the mantle and plate. The temperature perturbation was placed at mid-depth. In Fig. 10 we plot the maximum stress difference, $\sigma_{\max}$, as a function of the wavelength of the sinusoidal temperature perturbation for various viscosity jumps. These results indicate that the presence of a 100 km deep high-viscosity layer at the upper surface (our model plate) results in an increase in $\sigma_{\max}$ by approximately 25 per cent. Moreover, it can be seen that the shape and peak of the stress response of the plate to a temperature perturbation of a given magnitude changes relatively little once the plate viscosity is greater than six times the viscosity in the layer. Based on this result, it appears as though using a larger viscosity jump in the numerical model will not change the results significantly and, therefore, the viscosity jump of 10 used in our numerical models captures the effects of rigid plates on surface stress differences. It can also be seen that when scaled to the depth of the mantle, a disturbance with a wavelength of 3500 km produces the largest lithospheric stresses for a given amplitude of the anomaly. This wavelength is close to the depth of the mantle and is likely the wavelength that drives the most vigorous flow, producing the largest surface stresses. Scaled to the mantle, a thermal perturbation of this wavelength produces a lithospheric stress of 0.23 MPa per degree K of the anomaly (scaling assumes $g = 10$ m s^{-2}, $\alpha = 2.5 \times 10^{-5}$ K^{-1}, mantle depth $= 2.89 \times 10^6$ m, $\rho = 4000$ kg m^{-3}). Hence, one would need a temperature anomaly of 339 K to produce the breaking threshold stress.

In Fig. 11 we show the maximum stress as a function of wavelength for different values of the curvature (r_s/r_c) calculated using a spherical model and a viscosity jump of 10. It can be seen that the maximum stress is decreased by approximately 40 per cent for the case

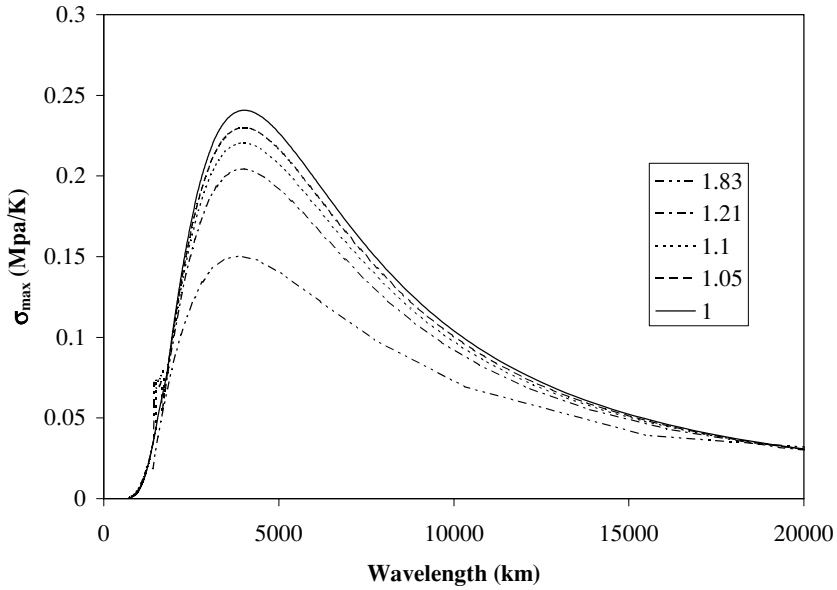

Figure 11. $\sigma_{\max}$ as a function of the azimuthal wavelength of the temperature perturbation for various values of the curvature (r_s/r_c) of the domain.

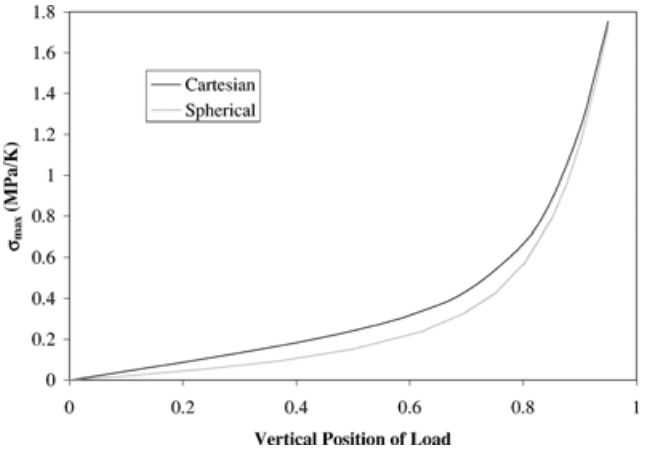

Figure 12. $\sigma_{\max}$ as a function of the height of the temperature perturbation above the CMB for a Cartesian model and a model with Earth-like curvature. $\sigma_{\max}$ is taken for the wavelength with the maximum stress difference.

of Earth-like curvature ($r_s/r_c = 1.83$) from its value when Cartesian geometry is used ($r_s/r_c = 1$). A temperature anomaly of 516 K is now needed for plate fracture. The wavelength that most efficiently induces stress is also decreased somewhat to 3000 km.

We investigated the mechanism responsible for the decrease in stress-difference generation by considering the effects of placing the temperature perturbation at different heights above the CMB in Cartesian and spherical geometries (a value of $r_s/r_c = 1.83$ was used for the spherical calculation). We calculated the maximum stress as a function of wavelength at each depth. The results are shown in Fig. 12; it can be seen that except when the perturbation is near either surface, the Cartesian calculation results in significantly higher surface stresses. This effect is related to the divergence of radial vectors in spherical geometry. Harmonic temperature perturbations drive an instantaneous flow in the form of periodic pairs of counter rotating cells bounded laterally by the planar and conical surfaces parallel to gravity in Cartesian and spherical geometry, respectively. Thus, in Cartesian geometry the wavelength of the surface stress perturbations is the same as the temperature perturbation at depth, whereas in spherical geometry the wavelength of surface stress perturbations is greater than that of the responsible temperature perturbations at depth. Diverging radial vectors in the latter case cause the buoyancy forces generated at depth to be spread over a larger surface area resulting in lower surface stresses. Taking an average of the difference between the two curves over the depth of the mantle, we estimate a total difference of 20 per cent.

5 DISCUSSION AND CONCLUSIONS

We have described a procedure for modelling the effects of surface tectonic plates in spherical axisymmetric geometry that preserves the plate-like aspect that vertical flow is limited to the plate boundary regions. The Gable *et al.* (1991) force balance approach has been used

previously by Monnereau & Quere (2001) in 3-D spherical geometry to examine the effects of surface plates on convection planform, surface heat flow and mantle temperatures. We have used this approach in our axisymmetric model to investigate the effects of various parameters on the generation of surface stresses.

The numerical modelling results indicate that it is extremely difficult to achieve the 80 MPa, average lithospheric stress that was used by Lowman & Jarvis (1996, 1999) as a criterion for supercontinent fracture. The results of the simple internal loading theory corroborate this finding; in either geometry, mass loads become significantly less effective in causing surface stresses as they increase in depth, but this is more pronounced in spherical geometry. As noted above, this is a result of the increase in surface area with height that occurs in spherical geometry, which is not captured in Cartesian geometry. For Earth-like curvature, the simple internal loading theory predicts a decrease of 20 per cent of the lithospheric stress difference caused by mass loads distributed over a range of depths. The internal loading theory also indicates that a factor of 10 viscosity discontinuity is sufficient to render the surface plate effectively rigid.

The Boussineq models and the model with no internal heating were noticeably cooler than the other model runs. However, no systematic trends of lithospheric stress with mantle temperature were apparent, arguing that the local buoyancy contrast between the descending plate and upper mantle was not the dominant factor in determining the magnitude of lithospheric stresses in these calculations.

It will also be noted that in our simulations that the continent is immobile, which is not the case for the Earth. Intuitively, one would expect that mobile continents would develop lower stresses than immobile ones because they may move so as to decrease surface stresses. This further reinforces our argument that calculated model stresses are too weak to fracture supercontinents. We have not considered the effects of variable viscosity in this study. There is a wide range of possible constitutive relations to describe the rheology of the mantle and plates (e.g. Bercovici 2003). Even simple depth and temperature-dependent rheologies include numerous ill-defined parameters. Investigations of these various parameter spaces will be deferred to future work. We can, however, make some general comments. If two simulations with the same convective vigour, as measured by surface heat flow or surface velocity are compared, one having an increase in viscosity with depth and one having constant viscosity, it is expected that the simulation with constant viscosity will develop larger surface stresses, simply as a result of its higher viscosity near the surface. We have shown that stress increases with viscosity for constant viscosity calculations and we expect this to be the case for depth-dependent viscosity calculations as well. The effect of temperature-dependent viscosity would be to soften plumes and stiffen slabs. This would tend to accentuate the viscous pull resulting from slabs and decrease surface stresses resulting from rising plumes.

Our results indicate that in a spherical Earth model, it is significantly more difficult to produce large surface stresses in supercontinents than was previously believed based on the results of Cartesian modelling efforts. The viscosity that we used was significantly higher than most estimates of mantle viscosity. Decreasing this viscosity would only further decrease surface stresses as we have demonstrated. The inclusion of phase transitions in our model results in an increase in the time dependence of the flow (compare models I.1 and I.4) primarily as a result of recurring avalanches of upper-mantle material into the lower mantle (e.g. Christensen & Yuen 1985; Machetel & Weber 1991; Tackley *et al.* 1993; Solheim & Peltier 1994; Butler & Peltier 2000). The associated surface stresses are, accordingly, more highly variable and reach higher peak values in model I.1 (with the phase transitions) than in model I.4 (without). For a lower viscosity and, therefore, higher (more Earth-like) Rayleigh number these avalanches may be more extreme and much larger surface stresses may occur. This will be the topic of future investigations. Although there is certainly significant uncertainty in the actual stress-difference that is necessary to fracture a super-continent, our results suggest that pre-existing weaknesses in the supercontinent may be necessary in order for supercontinent fracture to take place. This conclusion is in agreement with recent analyses of major rift systems by Tommasi & Vauchez (2001).

ACKNOWLEDGMENTS

We would like to thank A. Leitch, H. Schmeling and an anonymous referee for their thoughtful comments in reviewing this manuscript. We would further like to acknowledge Larry Solheim and W.R. Peltier whose numerical convection code we have further modified to perform the investigation described here. We would also like to thank the National Sciences and Engineering Research Council of Canada for their financial support.

REFERENCES

Adams, J.C., 1993. MUDPACK-2 - Multigrid software for approximating elliptic partial-differential equations on uniform grids with any resolution, *Appl. Math. Comput.,* **53,** 235–249.

Bercovici, D., Schubert, G. & Glatzmaier, G.A., 1989a. Three-dimensional spherical models of convection in the Earth's mantle, *Science,* **244,** 950–955.

Bercovici, D., Schubert, G. & Glatzmaier G.A., 1989b. Influence of heating mode on three-dimensional mantle convection, *Geophys. Res. Lett.,* **16,** 617–620.

Bercovici, D., 2003. The generation of plate tectonics from mantle convection, *Earth planet. Sci. Lett.,* **205,** 107–121.

Bott, M.H.B., 1976. Formation of sedimentary basins of graben type by extension of the continental crust, *Tectonophysics,* **36,** 77–86.

Brace, W.F. & Kohlstedt, D.L., 1980. Limits on lithospheric stress imposed by laboratory experiments, *J. geophys. Res.,* **85,** 6248–6252.

Butler, S.L. & Peltier, W.R., 1997. Internal thermal boundary layer stability in phase transition modulated convection, *J. geophys. Res.,* **102,** 2731–2749.

Butler, S.L. & Peltier, W.R., 2000. On scaling relations in time-dependent mantle convection and the heat transfer constraint on layering, *J. geophys. Res.,* **105,** 3175–3208.

Chandrasekhar, S., 1961. *Hydrodynamic and Hydromagnetic Stability*, Dover, New York, 652.

Chopelas, A., Boehler R. & Lo, T., 1994. Thermodynamics and behaviour of Mg_2SiO_4 at high pressure: Implications for $\gamma - Mg_2SiO_4$ phase equilibrium, *Phys. Chem. Min.,* **21,** 351–359.

Christensen, U. & Yuen, D.A., 1985. Layered convection induced by phase transitions, *J. geophys. Res.,* **90,** 10 291–10 300.

Condie, K.C., 1998. Episodic continental growth and supercontinents: a mantle avalanche connection?, *Earth planet. Sci. Lett.,* **163,** 97–108.

Dubuffet, F., Rabinowicz M. & Monnereau, M., 2000. Multiple scales in mantle convection, *Earth planet. Sci. Lett.,* **178,** 351–366.

Forte A. & Peltier, W.R., 1991. Viscous flow models of global geophysical observables; 1, Forward problems, *J. geophys. Res.,* **96,** 20 131–20 159.
Gable, C., O'Connell R.J. & Travis, B.J., 1991. Convection in 3 Dimensions with Surface Plates - Generation of Toroidal Flow, *J. geophys. Res.,* **96,** 8391–8405.
Ghebreab, W., Carter, A., Hurford, A.J. & Talbot, C.J., 2002. Constraints for timing of extensional tectonics in the western margin of the Red Sea in Eritrea, *Earth planet. Sci. Lett.,* **200,** 107–119.
Gurnis, M., 1988. Large-scale mantle convection and the aggregation and dispersal of supercontinents, *Nature,* **322,** 695–699.
Hager, B.H. & Clayton, R.W., 1989. *Constraints on the structure of mantle convection using seismic observations, flow models, and the geoid. In Mantle Convection: Plate Tectonics and Global Dynamcis,* ed. W.R. Peltier, Vol. 4 of The Fluid Mechanics of Astrophysics and Geophysics, Geodynamics Series. Gordon and Breach Science Publishers, New York, pp.657–763.
Haxby, W.F., Turcotte, D.L. & Bird, J.M., 1976. Thernal and mechanical evolution of the Michigan Basin, *Tectonophysics,* **36,** 55–75.
Ionov, D., 2002. Mantle structure and rifting processes in the Baikal-Mongolia region: geophysical data and evidence from xenoliths in volcanic rocks, *Tectonophysics,* **351,** 41–60.
Kohlstedt, D.L., Evans, B. & Mackwell, S.J., 1995. Strength of the lithosphere: constraints imposed by laboratory experiments, *J. geophys. Res.,* **100,** 17 587–17 602.
Jarvis, G.T., Glatzmaier, G.A. & Vangelov, V.I., 1995. Effects of curvature, aspect ratio and plan form in 2-dimensional and 3-dimensional spherical-models of thermal-convection, *Geophys. astrophys. Fluid Dyn.,* **79,** 147–171.
Lesne, O., Calais, E. & Deverchere, J., 1998. Finite element modelling of crustal deformation in the Baikal rift zone: new insights into the active-passive rifting debate, *Tectonophysics,* **289,** 327–340.
Lowman, J.P. & Jarvis, G.T., 1993. Mantle convection flow reversals due to continental collisions, *Geophys. Res. Lett.,* **20,** 2087–2090.
Lowman, J.P. & Jarvis, G.T., 1995. Mantle convection models of continental collision and breakup incorporating finite thickness plates, *Phys. Earth planet. Int.,* **88,** 53–68.
Lowman, J.P. & Jarvis, G.T., 1996. Continental collisions in wide aspect ratio and high Rayleigh number two-dimensional mantle convection models, *J. geophys. Res.,* **101,** 25 485–25 497.
Lowman, J.P. & Jarvis, G.T., 1999. Effects of mantle heat source distribution on supercontinent stability, *J. geophys. Res.,* **104,** 12 733–12 746.
Machetel, P. & Weber, P., 1991. Intermittent layered convection in a model mantle with an endothermic phase change at 670 km, *Nature,* **350,** 55–57.
Mckenzie, D.P., 1967. Some remarks on heat flow and gravity anomalies, *J. geophys. Res.,* **72,** 6261–6273.
McKenzie, D.P., 1978. Some remarks on the development of sedimentary basins, *Earth planet. Sci. Lett.,* **40,** 25–32.
Monnereau, M. & Rabinowicz, M., 1996. Is the 670 km phase transition able to layer the Earth's convection in a mantle with depth-dependent viscosity?, *Geophys. Res. Lett.,* **23,** 1001–1004.
Monnereau, M. & Quere, S., 2001. Spherical shell models of mantle convection with plate tectonics, *Earth planet. Sci. Lett.,* **184,** 575–587.
Nikishin, A.M., Ziegler, P.A., Abbott, D., Brunet, M.-F. & Cloetingh, S., 2002. Permo-Triassic intraplate magmatism and rifting in Eurasia: implications for mantle plumes and mantle dynamics, *Tectonophysics,* **351,** 3–39.
Peltier, W.R. & Jiang, X., 1996. Mantle viscosity from the simultaneous inversion of multiple data sets pertaining to post-glacial rebound, *Geophys. Res. Lett.,* **23,** 503–506.
Oxburgh, E.R. & Turcotte, D.L., 1968. Mid-ocean ridges and geotherm distribution during mantle convection, *J. geophys. Res.,* **73,** 2463–2661.
Rabinowicz, M., Ceuleneer G., Monnereau M. & Rosemberg, C., 1990. 3-dimensional models of mantle flow across a low-viscosity zone—implications for hotspot dynamics, *Earth planet. Sci. Lett.,* **99,** 170–184.
Sheth, H.C., 1999. A historical approach to continental flood basalt volcanism: insights into pre-volcanic rifting, sedimentation, and early alkaline magmatism, *Earth planet. Sci. Lett.,* **168,** 19–26.
Solheim, L. & Peltier, W.R., 1994. Avalanche effects in phase transition modulated thermal convection: A model of the Earth's mantle, *J. geophys. Res.,* **99,** 6997–7018.
Steinberger, B., Schmeling, H. & Marquart, G., 2001. Large-scale lithospheric stress field and topography induced by global mantle circulation, *Earth planet. Sci. Lett.,* **186,** 75–91.
Tackley, P.J., Stevenson, D.J., Glatzmaier, G.A. & Schubert, G., 1993. Effects of an endothermic phase transition at 670 km depth in a spherical model of convection in the Earth's mantle, *Nature,* **361,** 699–704.
Tommasi, A. & Vauchez, A., 2001. Continental rifting parallel to ancient collisional belts: an effect of the mechanical anisotropy of the lithospheric mantle, *Earth planet. Sci. Lett.,* **185,** 199–210.
Vangelov, V.I. & Jarvis, G.T., 1994. Geometrical effects of curvature in axisymmetrical spherical-models of mantle convection, *J. geophys. Res.,* **99,** 9345–9358.

APPENDIX A: DERIVATION OF BOUNDARY CONDITIONS AT A VISCOSITY DISCONTINUITY

In the same manner as Dubuffet *et al.* (2000) and Rabinowicz M. *et al.* (1990), we require that the velocity and the vertical components of the stress tensor be continuous across a viscosity discontinuity:

$$\Delta u_r = 0, \quad \Delta u_\theta = 0, \quad \Delta \tau_{r\theta} = 0, \quad \Delta \tau_{rr} = 0. \tag{A1}$$

Using eq. (13) and the fact that ρ_r, the background radial variation in density, is continuous, we can write the continuity of the two velocity fields as

$$\Delta \psi = 0 \tag{A2}$$

and

$$\Delta \frac{\partial \psi}{\partial r} = 0. \tag{A3}$$

The first relation can be derived from the continuity of the azimuthal derivative of the stream function. This condition tells us that the stream function on the upper and lower sides can differ by at most an additive constant and because the boundary condition on the axes of rotation forces the stream function to be zero there (a no flux condition), the stream function itself must be continuous.

The tangential stress in spherical coordinates can be written as

$$\tau_{r\theta} = \eta \left(\frac{r}{2} \frac{\partial}{\partial r} \left(\frac{u_\theta}{r} \right) + \frac{1}{2r} \frac{\partial u_r}{\partial \theta} \right). \tag{A4}$$

The condition on the tangential stress can then be written using the vorticity (eq. 14) as

$$\Delta\left[\eta\left(\frac{w}{2\sin\theta}+\frac{\partial u_r}{\partial\theta}-u_\theta\right)\right]=0. \tag{A5}$$

Because u_θ and $\frac{\partial u_r}{\partial\theta}$ are both continuous across the discontinuity in viscosity, we can write the discontinuity equation for the vorticity as

$$\Delta(\eta\omega)=2\sin\theta\left(u_\theta-\frac{\partial u_r}{\partial\theta}\right)\Delta\eta. \tag{A6}$$

When expanded, this gives an expression for the vorticity on the upper surface in terms of that on the lower surface (indicated by superscripts + and −, respectively):

$$\omega^+=\omega^-\frac{\eta^-}{\eta^+}+2\sin\theta\left(u_\theta-\frac{\partial u_r}{\partial\theta}\right)\Delta\eta/\eta^+. \tag{A7}$$

The radial normal component of the stress tensor takes the form

$$\tau_{rr}=-\frac{p}{\alpha_0\Delta T}+\eta\left(2\frac{\partial u_r}{\partial r}+\frac{2}{3\rho_r}\frac{\partial\rho_r}{\partial r}u_r\right). \tag{A8}$$

Here, we have also used the continuity equation for an anelastic fluid.

Because we do not have an explicit expression for the pressure, we differentiate eq. (A8) and apply the Δ operator to get

$$\Delta\frac{\partial p}{\partial\theta}=\left(2\frac{\partial^2 u_r}{\partial r\partial\theta}+\frac{2}{3\rho_r}\frac{\partial\rho_r}{\partial r}\frac{\partial u_r}{\partial\theta}\right)\Delta\eta\alpha_0\Delta T. \tag{A9}$$

Here we have used the fact that $\frac{\partial u_r}{\partial r}$ must be continuous because all of the other terms in eq. (1) are continuous across the viscosity discontinuity. We use the $\hat{\theta}$ component of the momentum equation to get an expression for $\frac{\partial p}{\partial\theta}$:

$$\frac{\partial p}{\partial\theta}=\left[\frac{1}{\sin\theta}\frac{\partial(\eta\omega)}{\partial r}+2\frac{\partial\eta}{\partial r}\left(\frac{\partial u_r}{\partial\theta}-u_\theta\right)-\frac{4\eta}{3\rho_r}\frac{\partial\rho_r}{\partial r}\frac{\partial u_r}{\partial\theta}\right]\alpha_0\Delta T. \tag{A10}$$

Applying the Δ operator to eq. (A10) and assuming that the first derivative of the viscosity is continuous, we get

$$\Delta\frac{\partial p}{\partial\theta}=\left[\frac{1}{\sin\theta}\Delta\frac{\partial(\eta\omega)}{\partial r}-\frac{4}{3\rho_r}\frac{\partial\rho_r}{\partial r}\frac{\partial u_r}{\partial\theta}\Delta\eta\right]\alpha_0\Delta T. \tag{A11}$$

Substituting eqs (A11) into(A9) gives us an equation for the discontinuity in the derivative of the vorticity:

$$\Delta\frac{\partial(\eta\omega)}{\partial r}=2\sin\theta\left(\frac{\partial^2 u_r}{\partial r\partial\theta}+\frac{1}{\rho_r}\frac{\partial\rho_r}{\partial r}\frac{\partial u_r}{\partial\theta}\right)\Delta\eta. \tag{A12}$$

If the viscosity is written as the sum of a continuous part, η_c, and a step discontinuity, $\Delta\eta\Theta(r-r_0)$, where Θ is the Heavyside step function and r_0 is the radius at which the discontinuity occurs, then eq. (A12) can be written

$$\frac{\partial\omega}{\partial r}^+=\frac{\eta^-}{\eta^+}\frac{\partial\omega}{\partial r}^--\frac{\partial\eta_c}{\partial r}\frac{\Delta\omega}{\eta^+}+2\sin\theta\left(\frac{\partial^2 u_r}{\partial r\partial\theta}+\frac{1}{\rho_r}\frac{\partial\rho_r}{\partial r}\frac{\partial u_r}{\partial\theta}\right)\Delta\eta/\eta^+. \tag{A13}$$

Approximating derivatives as fourth-order finite differences and combining eqs (A2) and (A3) we get

$$\begin{aligned}\psi_1^+=\psi_1^-=\Bigg[&48\left(\psi_2^+\frac{\partial X}{\partial r}^++\psi_2^-\frac{\partial X}{\partial r}^-\right)-36\left(\psi_3^+\frac{\partial X}{\partial r}^++\psi_3^-\frac{\partial X}{\partial r}^-\right)\\&+16\left(\psi_4^+\frac{\partial X}{\partial r}^++\psi_4^-\frac{\partial X}{\partial r}^-\right)-3\left(\psi_5^+\frac{\partial X}{\partial r}^++\psi_5^-\frac{\partial X}{\partial r}^-\right)\Bigg]\Bigg/\left[25\left(\frac{\partial X}{\partial r}^-+\frac{\partial X}{\partial r}^+\right)\right],\end{aligned} \tag{A14}$$

and combining eqs (A7) and (A13) we get

$$\begin{aligned}\omega_1^+=\Bigg[&48\left(\omega_2^+\eta^+\frac{\partial X}{\partial r}^++\omega_2^-\eta^-\frac{\partial X}{\partial r}^-\right)-36\left(\omega_3^+\eta^+\frac{\partial X}{\partial r}^++\omega_3^-\eta^-\frac{\partial X}{\partial r}^-\right)\\&+16\left(\omega_4^+\eta^+\frac{\partial X}{\partial r}^++\omega_4^-\eta^-\frac{\partial X}{\partial r}^-\right)-3\left(\omega_5^+\eta^+\frac{\partial X}{\partial r}^++\omega_5^-\eta^-\frac{\partial X}{\partial r}^-\right)\\&+\left(25A\frac{\partial X}{\partial r}^--12B\Delta x\right)\Bigg]\Bigg/\left[25\eta^+\left(\frac{\partial X}{\partial r}^-+\frac{\partial X}{\partial r}^+\right)\right],\end{aligned} \tag{A15}$$

and

$$\begin{aligned}\omega_1^-=\Bigg[&48\left(\omega_2^+\eta^+\frac{\partial X}{\partial r}^++\omega_2^-\eta^-\frac{\partial X}{\partial r}^-\right)-36\left(\omega_3^+\eta^+\frac{\partial X}{\partial r}^++\omega_3^-\eta^-\frac{\partial X}{\partial r}^-\right)\\&+16\left(\omega_4^+\eta^+\frac{\partial X}{\partial r}^++\omega_4^-\eta^-\frac{\partial X}{\partial r}^-\right)-3\left(\omega_5^+\eta^+\frac{\partial X}{\partial r}^++\omega_5^-\eta^-\frac{\partial X}{\partial r}^-\right)\\&-\left(25A\frac{\partial X}{\partial r}^++12B\Delta x\right)\Bigg]\Bigg/\left[25\eta^-\left(\frac{\partial X}{\partial r}^-+\frac{\partial X}{\partial r}^+\right)\right].\end{aligned} \tag{A16}$$

In the equation above,

$$A = 2\sin\theta\,\Delta\eta\left(u_\theta - \frac{\partial u_r}{\partial\theta}\right) \tag{A17}$$

and

$$B = 2\sin\theta\,\Delta\eta\left(\frac{\partial^2 u_r}{\partial r\,\partial\theta} + \frac{1}{\rho_r}\frac{\partial\rho_r}{\partial r}\frac{\partial u_r}{\partial\theta}\right), \tag{A18}$$

and the superscripts $+$ and $-$ indicate that a quantity is evaluated above or below the surface of the discontinuity, while the subscripts indicate the number of grid points from the discontinuity. The variable X allows us to use a different grid spacing in the sublithospheric mantle and in the plate. If the same spacing were used in both regions then $\frac{\partial X}{\partial r}^{+} = \frac{\partial X}{\partial r}^{-} = 1$.